CEAS Aeronautical Journal
https://doi.org/10.1007/s13272-023-00679-6

ORIGINAL PAPER

A contribution to the investigation of acoustic interferences in aircraft distributed propulsion

Sébastien Guérin[1] · **Damiano Tormen**[2]

Received: 27 February 2023 / Revised: 15 August 2023 / Accepted: 21 August 2023

Abstract
The objective of this work is to better understand the acoustic interferences created by distributed propulsion engines based on an approach that combines RANS simulation results for the aerodynamic prediction and analytical models to calculate acoustics. A multi-propeller configuration without wing is considered for this investigation. The propeller geometry and the operating conditions are realistic for a regional transport airplane. In the first part of the paper, the results obtained by two different and independent prediction methods are compared. One method is well-established and serves as validation for the second, low-order method, which is better suited for design-to-noise applications since it requires less details as input and is computationally faster by several orders of magnitude. The good agreement between both methods, obtained for a single propeller as well as for the distributed propeller configuration, is exploited in the second part of the paper to investigate the role of acoustic interferences. Taking acoustic interferences into account drastically affects the directivity of the tonal emission. Compared to the results obtained by considering the propellers as if they were uncorrelated, the far-field sound pressure levels can be significantly lower at the radiation nodes or amplified up to the theoretical limit of 9 dB calculated for eight propellers. The directivity patterns depend on the relative initial angular positions of the propellers. When these positions are randomly varied according to the uniform probability density distribution model, the mean result (expectation) is the same as if the propellers were considered as uncorrelated. Finally, the results show that the probability that the acoustic level is lower than the mean value is higher than 50% because of the positive skewness of the probability distribution of the resulting pressure amplitude. Even though the propeller–propeller and propeller–wing interactions were not considered, the essence of the findings is expected to remain valid for more complex configurations because those interactions are rotor phase-locked.

Keywords Hybrid-electric propulsion · Distributed propulsion · Propeller noise · Acoustic interferences · Reduced-order modeling

1 Introduction

As a reaction to the extremely concerning earth global warming resulting from the high level of anthropogenic emissions, for which the CO_2 emission as a product of fossil fuel combustion [1] is mostly responsible, the aeronautic community has launched a series of projects aiming to investigate alternative propulsion systems to reduce the environmental impact of aviation. In this perspective, the distributed electric propulsion (DEP) has gained increasing interest in the last decade. The principle of DEP consists in splitting the total thrust among many propulsors and distribute them over the airframe, offering novel possibilities for aircraft design oriented to lowering the emissions. Reviews of the distributed electric propulsion concepts and their potential advantages are presented by Kim et al. [2]. One of the solutions considered for regional transport aircraft relies on DEP with hybrid-electric propulsion. The European project IMOTHEP [3] has the ambition to assess the potential of such concepts and push their development. We must recognize the fact that the potential of some of the technologies is still uncertain at present. A solution that uses distributed

✉ Sébastien Guérin
sebastien.guerin@dlr.de

Damiano Tormen
damiano.tormen@ait.ac.at

[1] Institute of Propulsion Technology, Deutsches Zentrum für Luft- und Raumfahrt, Müller-Breslau-Str. 8, 10585 Berlin, Germany

[2] Center for Low-Emission Transport, AIT Austrian Institute of Technology GmbH, Giefinggasse 2, 1210 Vienna, Austria

Published online: 20 September 2023

propellers as propulsion system for regional aircraft is under investigation in the framework of the project. The choice of using propeller engines comes from the lower flight speed requirement, which is a further mean to reduce the overall energy consumption.

Several studies are already available in literature concerning the preliminary design of DEP architectures at aircraft level [5–8]. The distributed propeller aerodynamics has been studied in recent years both numerically [9–11] and experimentally [12]. The aeroacoustics of interacting distributed propellers or fans has also been studied using numerical approaches [11, 13, 14]. The aim of the existing studies has been to assess aeroacoustic effects typical of interacting DEP and to develop tools for the low-noise design. However, interaction effects are still relatively unexplored and further investigations are needed to shed light on the physical mechanisms and the complex acoustic interference patterns.

In their study on the impact of distributed propulsion on engine noise, Guérin et al. [4] considered that all the fan sources were not interfering one with each other and could be considered as uncorrelated acoustic sources. For propellers, whose noise signature is strongly dominated by the tones, this hypothesis may be less appropriate since the interference between the waves can produce strong variations of the directivity patterns. Pascioni and Rizzi [13] focused their numerical study on the tonal noise emitted by distributed propellers on an unmanned aerial vehicle, demonstrating the high impact of propeller tonal noise interferences. They found that the initial propeller rotation phases have a major impact on the noise directivity and intensity. By performing a statistical study with random initial propeller phases, they estimated the average noise emission, the probability distribution function, and the variation. They demonstrated the potential effectiveness of the propeller phase control as noise reduction means. However, without any control means, the relative propeller phasing is random and unknown, making representative noise predictions very challenging, especially if many propellers must be considered. The project IMOTHEP offers the opportunity to investigate the interference effects on the example of a regional platform with eight distributed propellers. For this principle study, the installation effects and the propeller-to-propeller interaction are not considered. The importance of propeller–wing interaction depends on many parameters, among which are the propeller geometry, the relative position between the propeller and the wing, the shape of the wing, and the propeller loading. Several investigations showed in the past that propeller noise is dominant for the fundamental blade passing frequency (BPF), in particular in the propeller plane. The installation effects are more important at the low and high emission angles [15]. As the BPF harmonic order rises, the role of the interactions becomes dominant because the amplitude of the propeller-alone tones rapidly decreases due to the weak radiation efficiency of the corresponding spinning modes.

In this paper, the noise emission from the eight propellers is predicted at two operating conditions, take-off and initial climb. RANS calculations for a single isolated propeller are used as starting point. Aerodynamic propeller-to-propeller and propeller–wing interactions are not considered. The main focus is put on the discrete tones radiated by the propellers, as they represent the dominant noise source at the vertical of the airplane as aforementioned. Two acoustic prediction methods are used, whose workflows are shown in Fig. 1. The first method—referred to as method 1—is computationally intensive as it uses a coupled Reynolds-Averaged Navier–Stokes–Ffowcs-Williams–Hankings (RANS–FWH) approach. The second one—referred to as method 2—relies on reduced information extracted from the RANS results as input and uses a simplified frequency-domain formulation of FWH, which runs several orders of magnitude faster. The first method is mainly used to validate the second one. Method 2 is further applied to identify and analyze acoustic effects of the distributed propellers. The paper is organized as follows: At first, the airplane configuration is introduced as well as the RANS results of the propeller calculations. Then, the acoustic theory is presented. As next, the RANS postprocessing required for applying method 2 and the acoustic results from both methods are compared for a single propeller and then the multi-propeller configuration. After that, method 2 is applied to further investigate the acoustic interference effects created by the distributed propellers. A probability study is carried out to understand the importance of the initial relative positions of the propellers on the directivity patterns.

2 Investigated case

2.1 Propellers

The regional airplane investigated in IMOTHEP [3] is a radical configuration with eight wingspan-distributed propellers as shown in Fig. 2. All propellers are identical. The propeller blade geometry created by the SAFRAN company during the first design iteration loop of the project is used to conduct the Reynolds-averaged Navier–Stokes (RANS) simulations. Each propeller has five blades and a diameter of approximately 2.6 m. It is assumed that each propeller is operated at the same speed and produces the same thrust. The position of the propellers result from the design at airplane level. The propeller positions are illustrated in Fig. 2 and the coordinates in the chosen airplane reference frame are provided in Table 4 in Appendix. The considered propeller rotational directions (in-board up) are also indicated in Fig. 2.

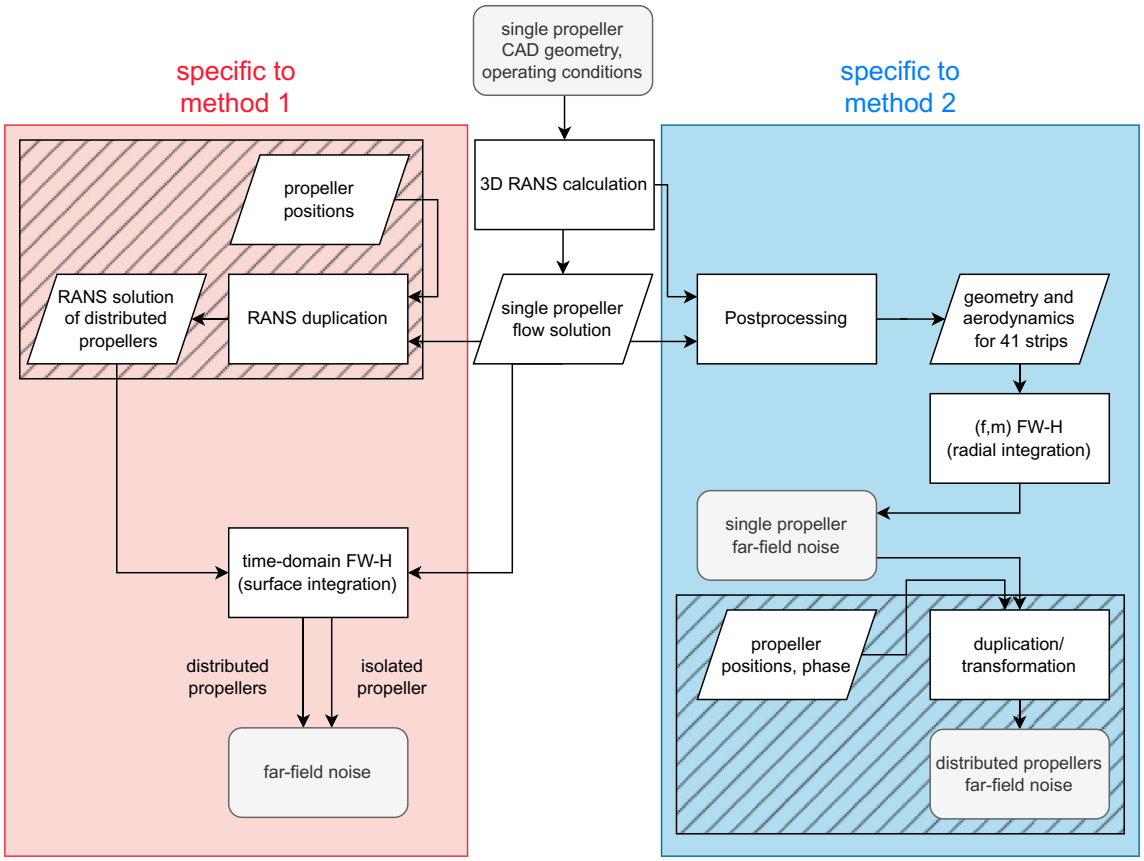

Fig. 1 Workflow of both methods applied in this work; the dashed areas encompass the tasks specific to the multi-propeller configuration

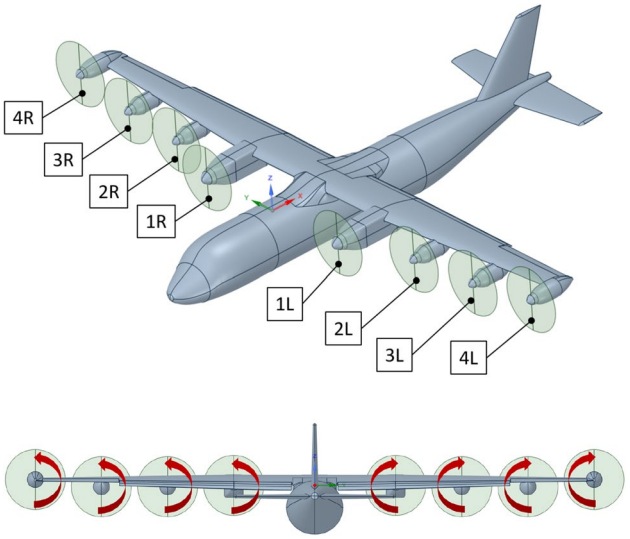

Fig. 2 Investigated airplane configuration with distributed propulsion; (top) nomenclature to identify the propellers, (bottom) direction of rotation of the propellers

Table 1 Investigated flight conditions

Operating point	Altitude (ft)	ISA	Mach	Propeller rpm	Blade pitch angle at 0.75*R*
TO	0	Yes	0.167	1500	27.59°
CL1	1500	Yes	0.31	1350	40.65°

2.2 Operating points

Two flight phases are considered in the present study: (1) take-off (TO) and (2) initial climb (CL1). The simulated flight conditions and the reference propeller speeds are indicated in Table 1.

2.3 Steady-state RANS predictions

For this study, the steady RANS simulations were performed for an isolated propeller, that is, the aerodynamic propeller-to-propeller interaction and the interaction with external geometries such as the wings and the fuselage are neglected.

Furthermore, the propellers are not inclined with respect to the incoming mean flow.

The flow field was computed by means of the commercial software ANSYS Fluent. A pressure-based 3D Navier–Stokes solver was used, with the $k-\omega$ SST turbulence model. The computational grid generation and flow field computations were done according to in-house best practices [16]. The computational domain extends for 15 and 25 rotor radii upstream and downstream the propeller plane, respectively, while its radial extent is 15 rotor radii. An unstructured polyhedral mesh was adopted. Prismatic cells at the blade and nacelle walls were adopted to properly compute the flow field in the boundary layer region. To reduce the computation demand, single blade passage simulations were performed by imposing periodic boundary conditions at the lateral surfaces of the computational domain. The resulting total grid cell number is 7.67 million. The blade pitch angles specific for TO and CL1 were different. Figure 3 shows the blade geometry and the rotation direction used in the CFD calculations. Figure 4 depicts contours of the blade surface pressure distribution obtained from CFD. The propeller performance was checked in terms of thrust, torque, and efficiency predicted for both operating points. The deviation with respect to the SAFRAN lifting line approach (considered as design operating point) was verified. At TO condition, the deviation is lower than 2%. For CL1, the largest deviation of −3.11% was observed for the propeller thrust prediction, while for torque and efficiency, the deviations were lower than 1.7%. Since the discrepancies obtained between predicted and design propeller performances are small, the CFD results were considered representative of the investigated flight conditions in terms of global aerodynamic loads. Therefore, the predicted flow fields were considered reliable for the purpose of this work.

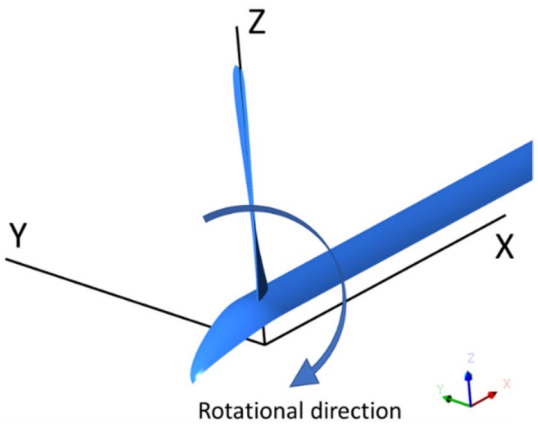

Fig. 3 Geometry and rotation direction of the single propeller blade passage of the CFD simulations (pitch angle at TO)

3 Acoustic prediction methods

3.1 Isolated propeller

3.1.1 Method 1: time-domain FW–H surface integration

The acoustic results of the so-called method 1 are obtained by means of the Ffowcs-Williams and Hawkings (FWH) acoustic analogy approach implemented in ANSYS Fluent, resolved in the Brentner and Farassat formulation [17]. The Fluent numerical implementation of FWH adopts a time-domain surface integral formulation wherein time histories of acoustic signals at prescribed receiver locations are directly

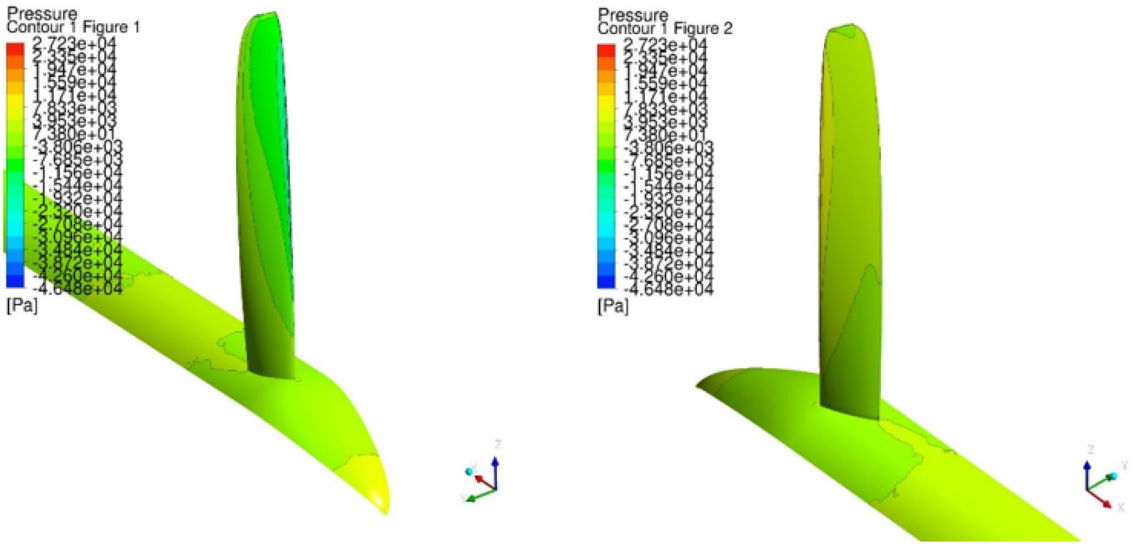

Fig. 4 Blade pressure distribution from RANS calculation at TO; (left) suction side, (right) pressure side

computed by evaluating corresponding surface integrals. In the present work, the blades rotate at subsonic speed. The blade solid surface was considered for integration of the equivalent acoustic sources. Therefore, only the blade thickness (monopole) and loading (dipole) contributions to the noise emission were considered, whereas the volume (quadrupole) sources were neglected. Since the steady RANS approach was adopted, the broadband noise contribution is not available and only the tonal noise components emitted at multiples of the blade passing frequency (BPF) were calculated. The airflow convective effects were also included in the noise computations. For single blade passage simulations, Fluent is capable of reconstructing the periodicity of the emitting surfaces, and thus accounts for the contribution of all the blades. The acoustic time history computed using Fluent is finally processed via discrete Fourier transform (DFT) to compute the acoustic signal in the frequency domain.

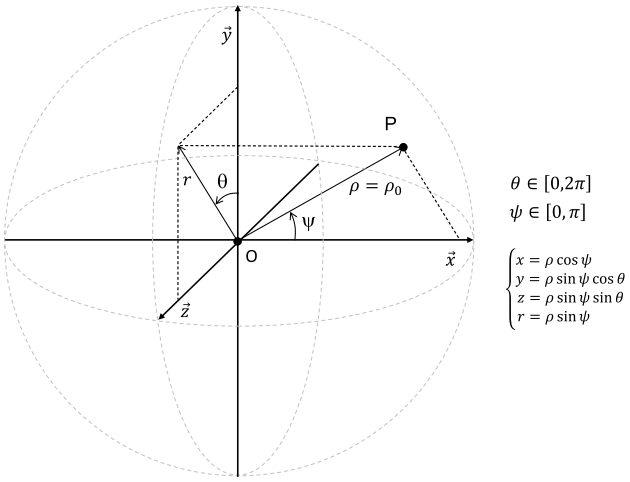

Fig. 5 System of coodinates as used for method 2

3.1.2 Method 2: simplified frequency domain FW–H radial integration

The second method is implemented in the DLR in-house code PropNoise. The theoretical derivation of the method can be found in Moreau and Guérin [18] or Moreau [19]. This approach is also based on the FWH analogy but has been simplified so that a fully analytical calculation is possible. Two main assumptions are applied: (i) the observer is located in the far-field and (ii) the blade is not cambered. Furthermore, the chordwise distributions of lift, drag, and thickness assume a typical shape, while the mean values are those obtained from the postprocessing of the RANS data as described later in Sect. 4.1.

Method 2 is briefly described hereafter. The spherical coordinate system (ρ, θ, ψ) with origin O shown in Fig. 5 is used to define the observer's position. The corresponding coordinates in the cylindrical and cartesian coordinate systems are indicated in Fig. 5.

The harmonic complex pressure emitted by a single propeller centered at $O = (0, 0, 0)$ can be written as follows:

$$p_{\omega,m}(\rho,\theta,\psi) = \breve{p}_{\omega,m}(\rho,\psi)e^{im\theta}. \tag{1}$$

For rotor-alone tones, the azimuthal order m is a multiple of the blade count B. It sign depends on the direction of rotation of the propeller. The acoustic pressure term $\breve{p}$ is calculated in the frequency domain, separately for each angular frequency ω and circumferential component m. The solution is reduced to a radial integration as shown in Ref. [18]:

$$\breve{p}_{\omega,m}(\rho,\psi) = e^{i(k_x x + k_r r)} \times B \int_{r_s=\eta R}^{R} \breve{g}_{\omega,m}(\rho,\psi,r_s) e^{-i(k_x x_{LE} + m\theta_{LE})} \sigma_{\omega,m}(r_s) dr_s, \tag{2}$$

where σ denotes the source term, $\breve{g}$, the free-field Green's function, R, the blade radius, and η, the hub-to-tip ratio. The variable r_s denotes the radial position of the blade segment and (x_{LE}, θ_{LE}) its leading edge coordinates. The Green's function reads

$$\breve{g}_{\omega,m}(\rho,\psi,r_s) = \frac{i^m}{4\pi\rho} \frac{J_m(k_r r_s)}{\sqrt{1 - M_x^2 \sin^2\psi}}, \tag{3}$$

with J_m, the Bessel function of first kind, and M_x, the axial Mach number. The axial wavenumber k_x is given by

$$k_x = \frac{k}{(1 - M_x^2)} \left(-M_x + \frac{\cos\psi}{\sqrt{1 - M_x^2 \sin^2\psi}} \right) \tag{4}$$

and the radial wavenumber k_r by

$$k_r = k \frac{\sin\psi}{\sqrt{1 - M_x^2 \sin^2\psi}}. \tag{5}$$

The source term σ depends on the source mechanism. For steady thickness noise, it corresponds to

$$\sigma^T_{\omega,m}(r_s) = k_l^2 c^2 \cdot \Psi^T \cdot \varrho_0 W_u \frac{\bar{t}}{c}, \tag{6}$$

and for steady loading noise, to

$$\sigma^L_{\omega,m}(r_s) = k_n c \cdot \Psi^L \cdot \frac{1}{2} \varrho_0 W_u^2 C_L. \tag{7}$$

In the last two equations, k_l and k_n are the chordwise and chord-normal wavenumbers, c ist the blade chord, Ψ is the Fourier transform of the normalized chordwise distribution of thickness (resp. loading) as introduced by Hanson [20], ϱ_0

is the mean flow density, W_u is the relative velocity upstream of the propeller, $\bar{t}$ is the mean blade thickness, and C_L is the lift coefficient.

Notice that a first comparison between a fully numerical and the RANS-informed acoustic prediction computed using method 2 has already been done for contra-rotating propellers [21]. A very good agreement was found for the tones generated by both propellers.

Even though broadband noise is not the focus of this work, it was calculated. The used method relies on the Willmarth and Roos [22] surface pressure spectrum modified by Moreau [19] to account for the blade loading via the drag coefficient C_D.

3.2 Distributed, fully-correlated propellers

A comparison for the case where the distributed propellers are considered as fully-correlated noise sources is also performed. In this case, the acoustic signals emitted by the eight propellers have to be added while the difference in phase is considered. Therefore, the position of the propellers with respect to the receivers must be considered. The coordinates of each propeller disk center in the receivers' cartesian reference frame are given in Table 4.

3.2.1 Method 1: direct calculation with all propellers

In method 1, the FWH solver is fed directly with eight propeller CFD solutions, practically obtained by replicating and consistently re-positioning in space the isolated propeller solution previously computed. The actual rotational directions of the propellers on both wings (in-board up) were accounted for. To do so, the four CFD solutions positioned on the starboard wing were obtained by preliminarily mirroring the isolated propeller solution, which simulates the rotational direction of the port wing propellers (see Fig. 2). With this approach, the acoustic time signals emitted by the eight propellers are added directly by the FWH solver at the receivers' locations, accounting for the phase shifts resulting from the different source positions in space.

3.2.2 Method 2: re-use of single propeller acoustic calculation, transformation, and summation

In the second approach, the tonal noise radiated by the eight propellers is calculated by transforming and summing the acoustic solutions obtained for the isolated case.

The complex directivity $D_{\omega,m}(\rho_{ref},\psi)$ obtained along the polar arc at a constant distance of reference ρ_{ref} in the far field is what is available from the PropNoise calculation. To obtain the complex pressure at any observer's position on a sphere of radius ρ_{ref}, the following operation has to be performed:

$$p_{\omega,m}(x,r,\theta) = D_{\omega,m}(\rho_{ref},\psi)e^{i(k_x x + k_r r + m\theta)}. \tag{8}$$

When the propeller is no more centered, the complex pressure must be projected from the system of coordinates attached to the propeller ($\tilde{\mathbf{x}}$) to the absolute system of coordinates ($\mathbf{x}$). For simplicity, we assume that the center of the sphere $\Leftarrow S$), on which the observers are placed, is also the center of the airplane reference frame. The following projection must be carried out:

$$\mathbf{x} = \begin{pmatrix} x \\ r \\ \theta \end{pmatrix} = \begin{pmatrix} x \\ \theta \\ \psi \end{pmatrix} \mapsto \tilde{\mathbf{x}} = \begin{pmatrix} \tilde{x} \\ \tilde{r} \\ \tilde{\theta} \end{pmatrix} = \begin{pmatrix} \tilde{x} \\ \tilde{\theta} \\ \tilde{\psi} \end{pmatrix} = \mathbf{x} - \mathbf{x_s}, \tag{9}$$

with $\mathbf{x}_s$ the position of the propeller in the airplane frame. This projection is illustrated in Fig. 6. Three operations are carried out. They correspond to the terms put in brackets in Eq. 10:

- Term I: the complex directivity is interpolated to obtain its value for the appropriate polar angle.
- Term II: the amplitude (in far field) is corrected to account for the different propagation distance. It is assumed that the amplitude varies inverse proportionally to the propagation distance ρ.
- Term III: the phase is corrected to account for the shift in position as predicted by Eq. 8.

Thus, the pressure amplitude of the propeller with offset is given by:

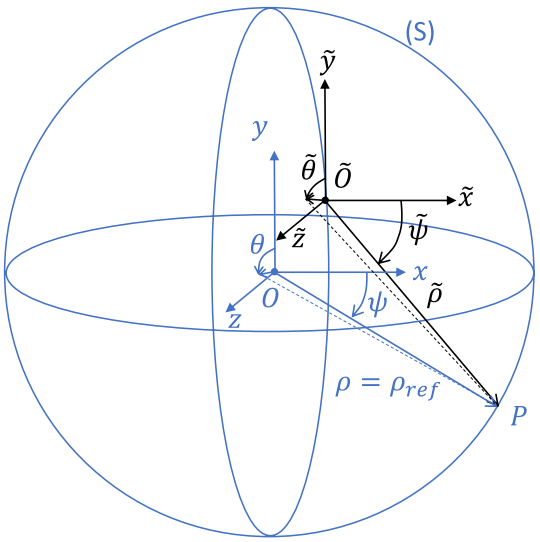

Fig. 6 Change of coordinates applied by method 2

$$p_{\omega,m}(\mathbf{x}) = \underbrace{D_{\omega,m}(\rho_{ref},\tilde{\psi})}_{I}\ \underbrace{\frac{\rho_{ref}}{\tilde{\rho}}}_{II}\ \underbrace{e^{i(\tilde{k}_x\tilde{x}+\tilde{k}_r\tilde{r}+m\tilde{\theta})}}_{III} \tag{10}$$

If the distance $\rho \equiv \rho_{ref}$, then in far field $\tilde{\rho} \approx \rho_{ref}$, hence

$$p_{\omega,m}(\mathbf{x}) \approx D_{\omega,m}(\rho_{ref},\tilde{\psi})e^{i(\tilde{k}_x\tilde{x}+\tilde{k}_r\tilde{r}+m\tilde{\theta})} \tag{11}$$

The operation is repeated for all the propellers and the results are summed:

$$p_{\text{all},\omega,m}(\mathbf{x}) = \sum_{\mu=1}^{8} p_{\mu,\omega,m(\mu)}(\mathbf{x}). \tag{12}$$

When propellers are counter-rotating, the sign of m is changed as the acoustic waves spins in the opposite direction.

Note that this method only applies to tonal noise. Broadband noise can be further considered uncorrelated as the source generation mechanism is triggered by the turbulence passing the trailing edge. Turbulence is stochastic by nature.

4 Results

4.1 RANS data reduction

Two sets of information were extracted from the RANS simulations to generate the input for method 2. The first data set contained the geometry and pressure distribution over constant radius blade profiles at 41 radial positions. The second data set provided the velocity profiles extracted upstream and downstream of the blade at about one chord from the leading and trailing edges. Those data were postprocessed to feed the method 2 with the required reduced parameters.

4.1.1 Velocities and flow angles

The axial positions of extraction of the velocity relative to the blade leading and trailing edges are shown in Fig. 7. The values upstream and downstream are extracted at the same radius.

The velocities $\mathbf{U} = (U_x, U_r, U_\theta)$ in the absolute cylindrical reference frame were provided along arcs at constant radius. The azimuthal range covers one blade passage. The raw data are showed in Fig. 8 for the TO condition.

Mean velocity values were calculated for each radial position. The fact that the points were not equidistant in azimuth was considered in the calculation. The required flow angles were determined after averaging. In the two-dimensional system of coordinates attached to the blade, the velocity becomes $\mathbf{W} = (W_x, W_\theta)$, with $W_x = U_x$ and $W_\theta = U_\theta + \Omega r$. Later, the flow deviation is used to cross-check the extracted data. Its value is defined as the difference

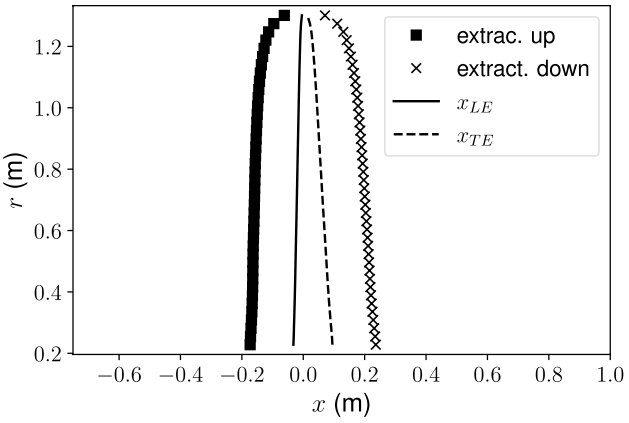

Fig. 7 (x, r)-positions of the data extraction with respect to the leading and trailing edges

between the tangential velocites measured upstream ($W_{\theta,u}$) and that obtained downstream ($W_{\theta,d}$):

$$\Delta W_\theta = W_{\theta,u} - W_{\theta,d} \tag{13}$$

The main results from this analysis are presented in Fig. 9.

4.1.2 Reduced geometry

Method 2 does not account for the detailed geometry of the blade as the acoustic equations are simplified. It only requires reduced parameters of the geometry (chord, mean thickness, camber, stagger angle at the leading and trailing edges, etc.), which are considered of first order importance for noise. Those parameters were obtained by analyzing the CFD extracted geometry of the blade profiles using a dedicated in-house program. Some of the important parameters are shown in Fig. 10. Note that the rough variations of the values of camber and stagger angles are related to the inaccuracy of the extraction method. They have a negligible effect on the acoustic results.

4.1.3 Lift and drag

The force produced by the propeller blades on the fluid was calculated by integrating the pressure distribution along the contours of the blade profiles. Then the lift and drag components were calculated using the perpendicular to the inflow angle to determine the direction of the lift at each radial position. An example of pressure distribution obtained at three radial positions is shown in Fig. 11.

The section lift coefficient C_L is calculated using the usual definition:

$$C_L = \frac{L}{0.5\rho_0 W_u^2 c}, \tag{14}$$

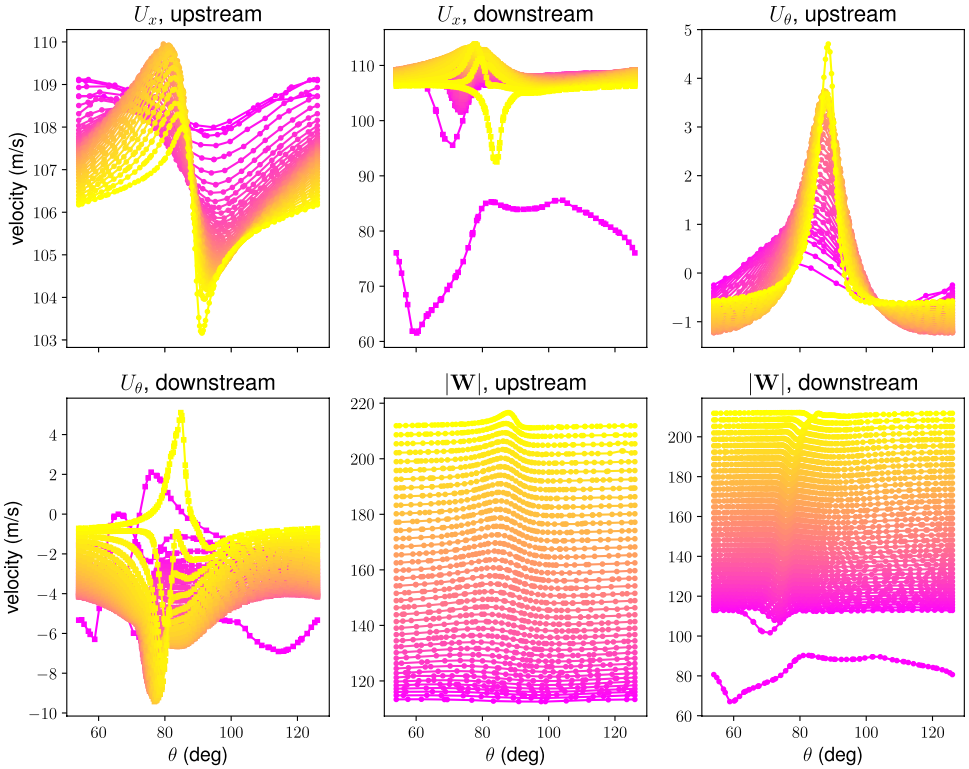

Fig. 8 Flow velocities extracted from the CFD data at TO condition; U_x axial velocity, U_θ absolute tangential velocity, $|\mathbf{W}| \equiv W = \sqrt{W_x^2 + W_\theta^2}$; colobar: values at the hub (pink), values at the tip (yellow)

where L is the lift, ϱ_0 is the mean flow density, W_u is the upstream velocity, and c is the blade chord. The same definition is used for the drag D. The radial evolution of lift and drag is shown in Fig. 12.

Finally, it was verified that the flow deviation calculated based on the lift coefficient (see Eq. 15) matches the one obtained directly from the RANS velocity field. A very good agreement between both solutions was found at TO and CL1 as can be seen in Fig. 13.

$$\Delta W_\theta = \frac{1}{2} C_L W_u \sigma \tag{15}$$

with σ, the blade solidity.

As final validation check, the forces were integrated radially to obtain the total thrust and the torque. The results, given in Table 2 for both operating points, are satisfactory with a discrepancy between method 1 (RANS) and method 2 (reduced RANS) lower than 2.5%.

4.2 Acoustic results

4.2.1 Uncorrelated-propeller assumption

A comparison by considering the distributed propellers as if they were fully uncorrelated sources was performed. This is a pure mathematical construct as two harmonic signals at the same frequency are necessarily perfectly correlated. In this case, the acoustic pressure in the propeller far field, denoted $p_\omega|_{\Sigma uncorr}$, is obtained by summing the amplitude of each signal as follows:

$$p_\omega^2|_{\Sigma uncorr} = N_p \cdot p_\omega^2, \tag{16}$$

In the preceding equation, p_ω is the root mean square of the acoustic pressure emitted by a single propeller, and N_p the number of propellers. The sound pressure level (SPL) for multiples of the BPF or for the overall signal is calculated with the standard definition:

$$SPL = 10 \log_{10} \left(p_{rms}^2 / p_{ref}^2 \right), \tag{17}$$

where p_{rms} is the root mean square pressure ($p_{rms}^2 = p_\omega^2/2$ for a single frequency) and $p_{ref} = 2 \times 10^{-5}$ Pa is the reference pressure.

The SPL directivities were calculated along a polar arc located in the far field at a distance equal to 100 propeller diameters ($\rho = 100 D_{prop} = 260$ m). A sketch of the adopted polar reference frame is illustrated in Fig. 14. The receiver position at polar angle $\psi_a = 90°$ lies in the rotating plane. For each arc, the positions $\psi_a = 0°$ and 180° indicate the upstream and downstream directions, respectively. Note that for a single propeller, the directivity is axisymmetric since only one azimuthal mode is triggered per tone.

The results obtained by both acoustic methods (method 1 and method 2) are compared in Fig. 15 for the first three BPF tones at TO and the BPF tone at CL1. The agreement is very

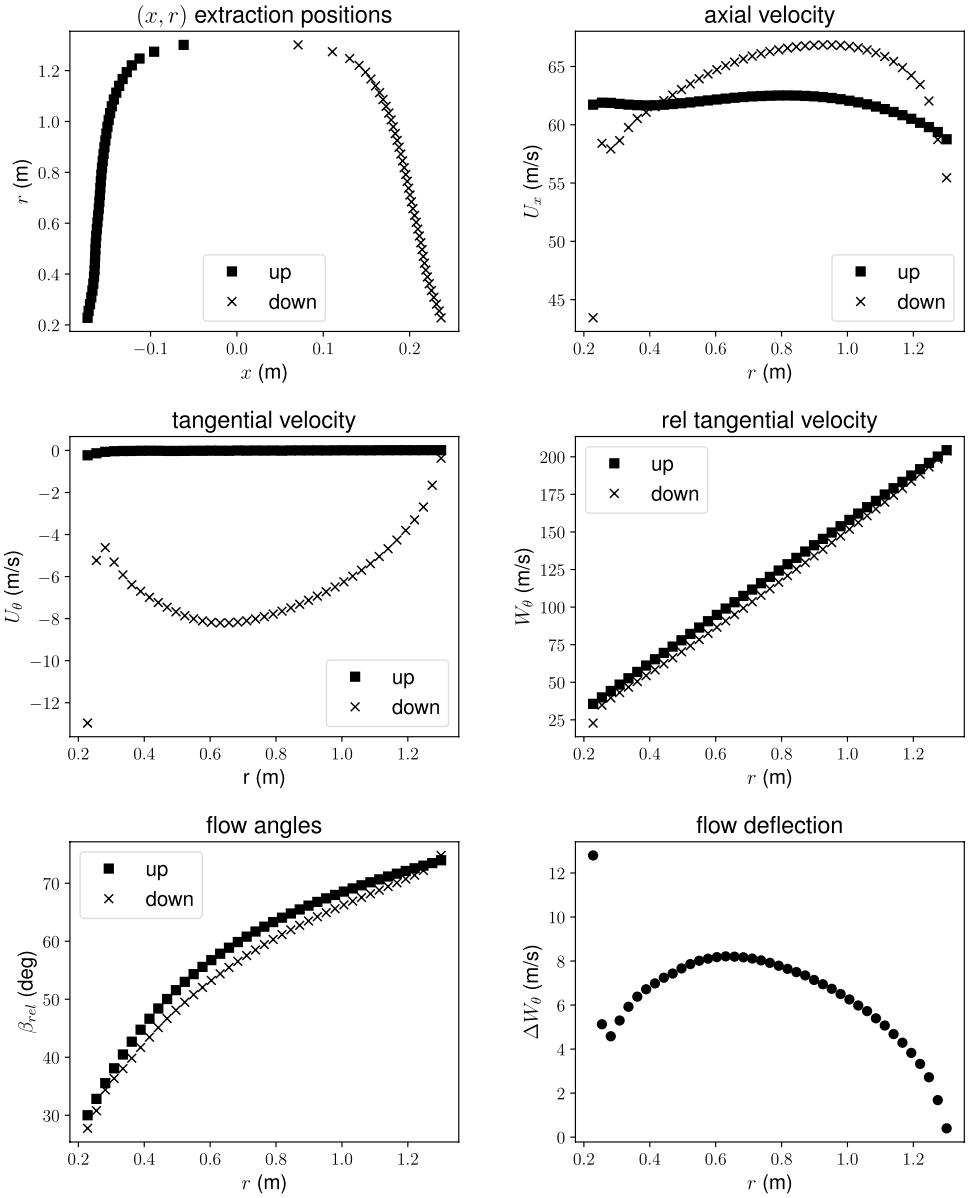

Fig. 9 Positions of CFD flow velocity extraction and mean velocity values (TO)

satisfactory (also for the other BPF tones at the condition CL1, whose directivities are not shown to avoid an overload of results). The steady loading noise is the main noise contributor at the two operating points. The maximum SPL value is located around $\psi_a = 100°$, that is, almost within the plane of the propellers. However, at angles lower than 60°, the thickness contribution dominates at the take-off condition. The offset between the two results is nearly constant for the three BPF, while directivity patterns are almost identical.

Method 2 predicts that the overall sound pressure levels (OASPL) obtained after summation of all the frequencies and all the sources are dominated by the propeller tones as it can be seen in Fig. 16. Only at the very low and high angles, broadband noise starts to be dominant. This observation has to be considered carefully as the interaction with the airframe, in particular the wings, is neglected.

In terms of OASPL but also in terms of sound power levels (OAPWL) (see Table 3), the propeller noise emission at take-off (TO) is slightly higher than at initial climb (CL1). This was expected as the propeller is operated with a higher load at TO.

4.3 Fully-correlated, distributed propellers

4.3.1 Definition of the initial angular position

The complex pressure emitted by a single propeller can be written in compact form as follows:

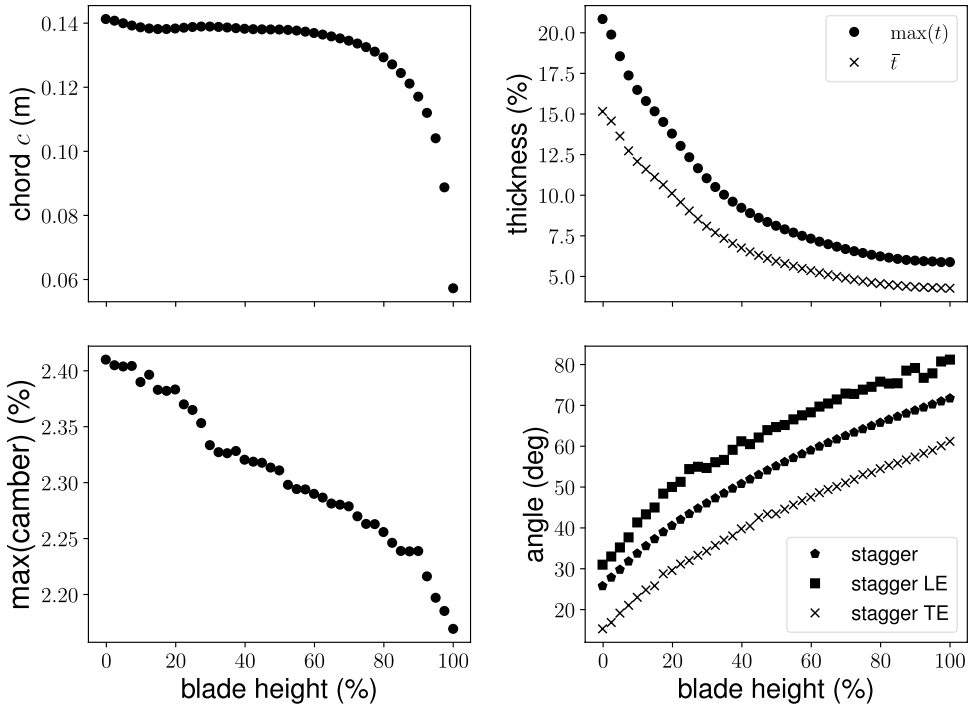

Fig. 10 Extracted parameters of the blade geometry (angles at TO)

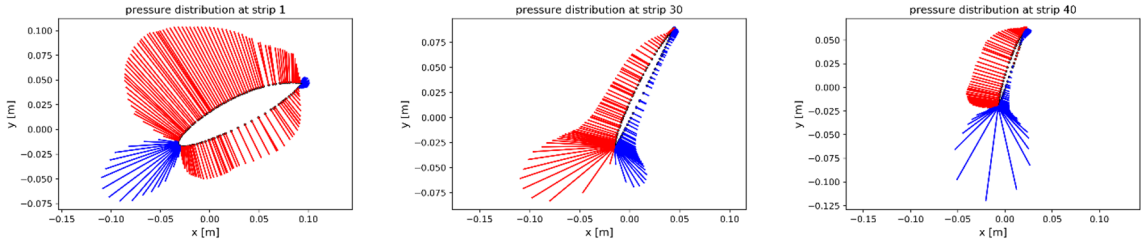

Fig. 11 Pressure distribution at three radial positions (hub, 75% radial span and near the tip); colors indicate the sign of the difference (red: positive, blue: negative) between the pressure on the blade surface and the ambient mean pressure; TO

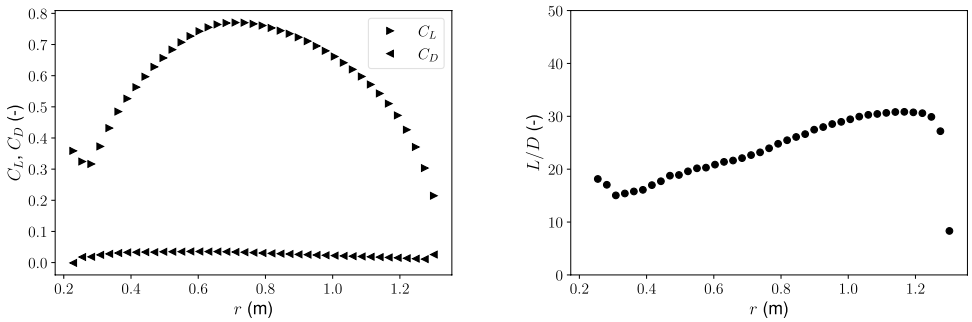

Fig. 12 Radial evolution of (left) the section lift and drag coefficients and (right) the lift-to-drag ratio; TO

Table 2 Calculated performance of one propeller

OP	Thrust (N)		Torque (Nm)	
	M1	M2	M1	M2
TO	4520.7	4544.6	2032.4	1981.3
CL1	2586.9	2634.7	2181.6	2128.7

$$p_\omega(\mathbf{x}) = De^{i\phi}e^{im\Delta\theta}, \tag{18}$$

where the phase ϕ is

$$\phi = \tilde{k}_x\tilde{x} + \tilde{k}_r\tilde{r} + m\tilde{\theta}. \tag{19}$$

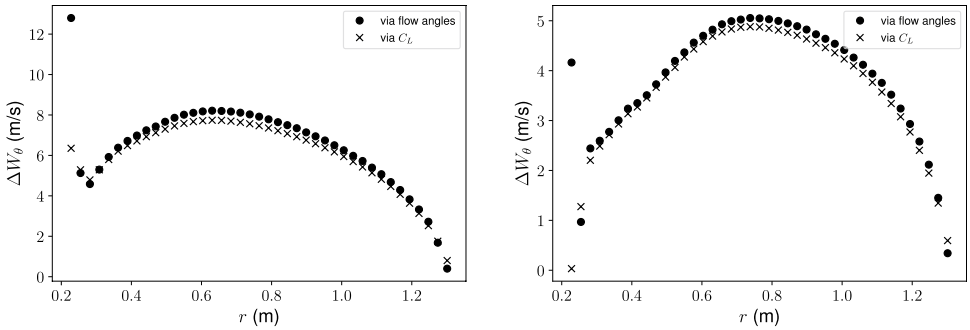

Fig. 13 Flow deviation as directly extracted from the RANS velocity data and reconstructed based on the C_L coefficient using Eq. 15: (left) TO, (right) CL1

In Eq. 18, the angle $\Delta\theta$ corresponds to the angular position of the propeller at a fictive reference time, e.g., at $t = 0$ (see illustration in Fig. 17). The concept of initial angular position is not relevant for a single propeller as its value only changes the phase of the signal but not its amplitude. However, for distributed propellers, this term is essential as the interference patterns depend strongly on its values as shown below.

The acoustic pressure emitted by all propellers together rotating at identical angular speed is given by:

$$p_\omega^2(\mathbf{x})|_{\Sigma corr} = \frac{1}{2} p_\omega(\mathbf{x})|_{\Sigma corr} \cdot p_\omega^*(\mathbf{x})|_{\Sigma corr} \tag{20}$$

$$= \frac{1}{2} \sum_{\mu}^{N_p} \sum_{\nu}^{N_p} p_{\omega,\mu}(\mathbf{x}) \cdot p_{\omega,\nu}^*(\mathbf{x}) \tag{21}$$

$$= \frac{1}{2} \sum_{\mu}^{N_p} \sum_{\nu}^{N_p} D_\mu D_\nu^* e^{i(\phi_\mu - \phi_\nu)} e^{im(\Delta\theta_\mu - \Delta\theta_\nu)}, \tag{22}$$

where the superscript $(*)$ denotes the complex conjugate value. In the following, it is assumed that all propellers have the same geometry and aerodynamic performance. Therefore, the same solution as for the case for uncorrelated propellers can be used for each propeller. Only the reference angular position can vary.

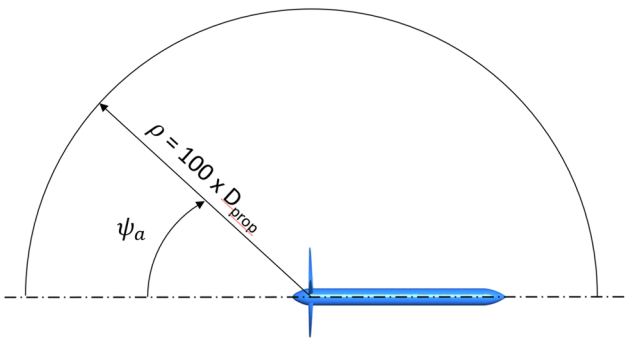

Fig. 14 Receivers' location along polar arc

4.3.2 Results for the same reference angular position

In this section, methods 1 and 2 are compared while the initial angular position is identical for all propellers (in this case $\Delta\theta_\nu = \pi/2, \forall\nu \in [1, 8]$). Due to interferences between the propellers, the noise directivity is no more axisymmetric. It has been decided to record the acoustic levels along the polar arcs illustrated in Fig. 18 located at five different azimuthal angles θ such as $\theta \in [\pi/2, -\pi/2]$. The distance to the aircraft remains equal to $100D_{prop}$. The results are shown in Fig. 19 for take-off (TO). (The same conclusion can be drawn for CL1.)

An excellent agreement between the two methodologies is obtained for all angular positions and frequencies. Not only the overall shape of the patterns is very similar, the position of the radiation nodes is the same, but also the absolute levels well agree. The 2 dB difference corresponds to that obtained for the single propeller already. The peak emission remains at the sideline position for $\psi_a \approx 100°$. Lobes typical of acoustic interferences are present in the directivity patterns. Compared to the results calculated with the uncorrelated assumption, there are azimuthal positions where the SPL values are significantly higher, by up to about 8 dB (e.g. at $\theta = 90°$ and $-90°$), and positions, where the levels are lower by several decibels. Theoretically, zero-pressure nodes can be present in the directivity pattern when the interference is perfectly destructive. Capturing this effect requires a fine discretization of the directivity since the amplitude drop in the vicinity of a node is very sharp. The adopted polar discretization here is $\Delta\psi_a = 0.5°$.

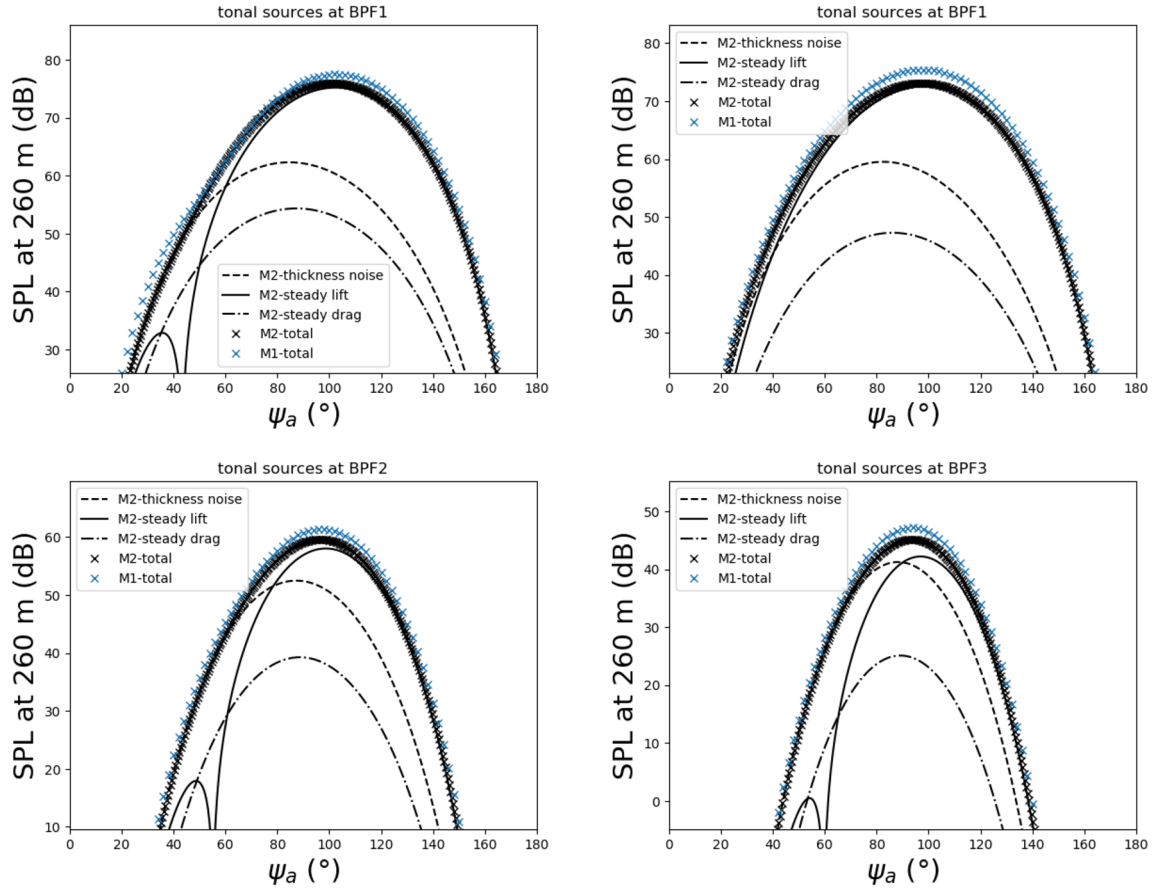

Fig. 15 Far-field pressure directivity: comparison at 260 m for eight propellers considered uncorrelated: (top left) BPF at TO, (top right) BPF at CL1, (bottom left) 2×BPF at TO, (bottom right) 3×BPF at TO

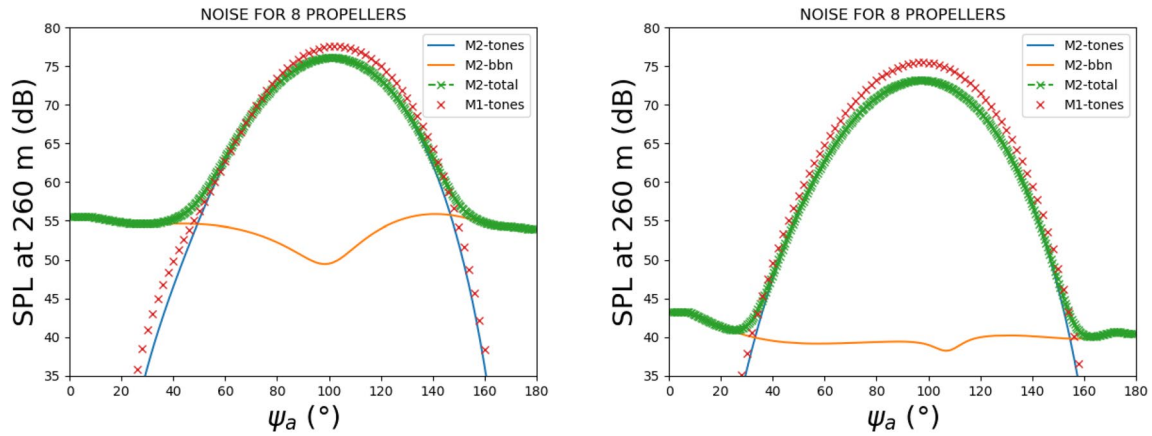

Fig. 16 OASPL: comparison at 260 m for eight propellers considered as uncorrelated: (left) TO, (right) CL1

Table 3 OAPWL obtained from method 2 (dB, ref. $= 10^{-12}$ W)

OP	TE bbn	Tones	TE bbn + Tones
TO	103.8 dB	120.9 dB	120.9 dB
CL1	89.7 dB	118.2 dB	118.2 dB

4.3.3 Importance of the propeller angular position

A real-time control of the relative angular position of the propellers can be thought as a solution to minimize the noise received on the ground. However, a noise reduction that occurs simultaneously at several observer positions does

Fig. 17 Definition of the angle $\Delta\theta$

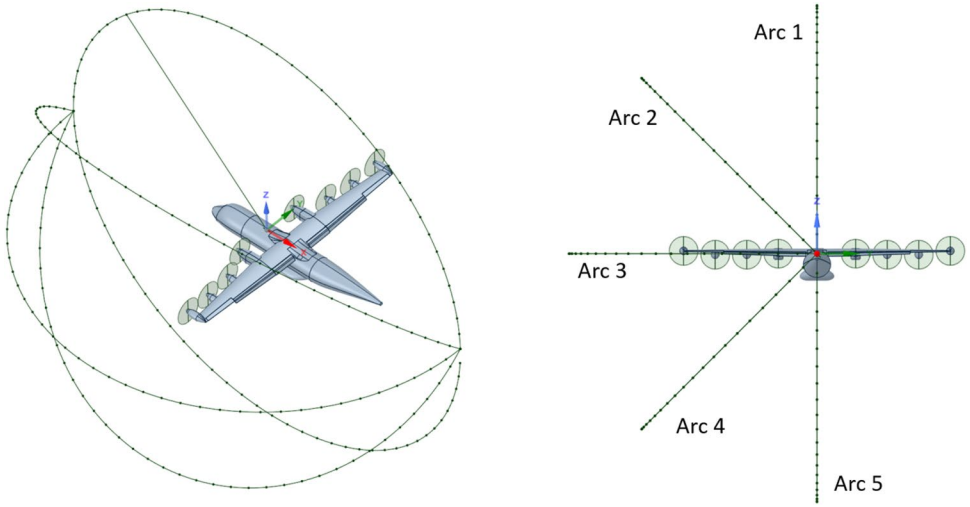

Fig. 18 Receivers' locations along five polar arcs considered in the correlated propeller simulations

not seem feasible in practice, as the solid angles with low noise are relatively small.

In this section, the effect of the position of the propellers relative to one another is appraised by means of a probability study.

First of all, a mean directivity is calculated. For that, the expectation in terms of pressure amplitude is calculated by setting the initial phase to random values (a uniform probability density fonction is assumed) and by repeating this operation for a number of trials Q, while Q tends to infinity:

$$\mathbb{E}[p_\omega^2(\mathbf{x})|_{\Sigma corr}] = \frac{1}{2Q}\lim_{Q\to\infty}\sum_{q}^{Q} p_\omega^2(\mathbf{x})^{(q)} \tag{23}$$

Combining this equation with Eq. (22) yields

$$\mathbb{E}[p_\omega^2(\mathbf{x})|_{\Sigma corr}] = \frac{1}{2Q}\lim_{Q\to\infty}\sum_{q}^{Q}\sum_{\mu}^{N_p}\sum_{\nu}^{N_p} D_\mu^* D_\nu e^{i(\phi_\mu-\phi_\nu)} e^{im(\Delta\theta_\mu^{(q)}-\Delta\theta_\nu^{(q)})}, \tag{24}$$

$$= \frac{1}{2}\sum_{\mu}^{N_p}\sum_{\nu}^{N_p} D_\mu^* D_\nu e^{i(\phi_\mu-\phi_\nu)}\frac{1}{Q}\lim_{Q\to\infty}\sum_{q}^{Q} e^{im(\Delta\theta_\mu^{(q)}-\Delta\theta_\nu^{(q)})}, \tag{25}$$

$$= \frac{1}{2}\sum_{\mu}^{N_p}\sum_{\nu}^{N_p} D_\mu^* D_\nu e^{i(\phi_\mu-\phi_\nu)}\mathbb{E}[e^{im(\Delta\theta_\mu-\Delta\theta_\nu)}]. \tag{26}$$

Two cases must be distinguished for the expectation term:

$$\mathbb{E}[e^{im(\Delta\theta_\mu-\Delta\theta_\nu)}] = 1 \quad \text{if } \nu=\mu, \tag{27}$$

$$= \mathbb{E}[e^{im\Delta\theta_\mu}]\cdot\mathbb{E}[e^{-im\Delta\theta_\nu}] = 0 \quad \text{if } \nu\neq\mu. \tag{28}$$

Two properties are used to justify that the second term is null in the last equation: 1) the random variables $\Delta\theta_{\mu,\nu}$ are independent and 2) the expectation of the cosine and sinus functions of a uniform distribution of random variable is null. This yields the following result:

$$\mathbb{E}[p_\omega^2(\mathbf{x})|_{\Sigma corr}] = \sum_{\mu}^{N_p} p_{\omega,\mu}^2(\mathbf{x}) = p_\omega^2|_{\Sigma uncorr}, \tag{29}$$

where $p_\omega^2|_{\Sigma uncorr}$ has been defined in Eq. 16. That is, the expected mean value for correlated propellers is equal to the uncorrelated propeller assumption. To verify this result and also quantify the variations in the directivity patterns, it was decided to perform 200 simulations with initial random phases for each of the initial propeller angles. The distribution of the angles is shown in Fig. 20. Ideally, the distribution of phase should be uniform but a larger number of trials should be necessary to reach a better convergence. Note that the simulation set was performed only using method 2 in light of its very low computation time.

The results of this probability study are shown in Fig. 21. First, they validate the theoretical finding: the mean directivity obtained for correlated sources and the directivity for uncorrelated sources overlap almost perfectly (compare blue solid lines and red dashed lines).

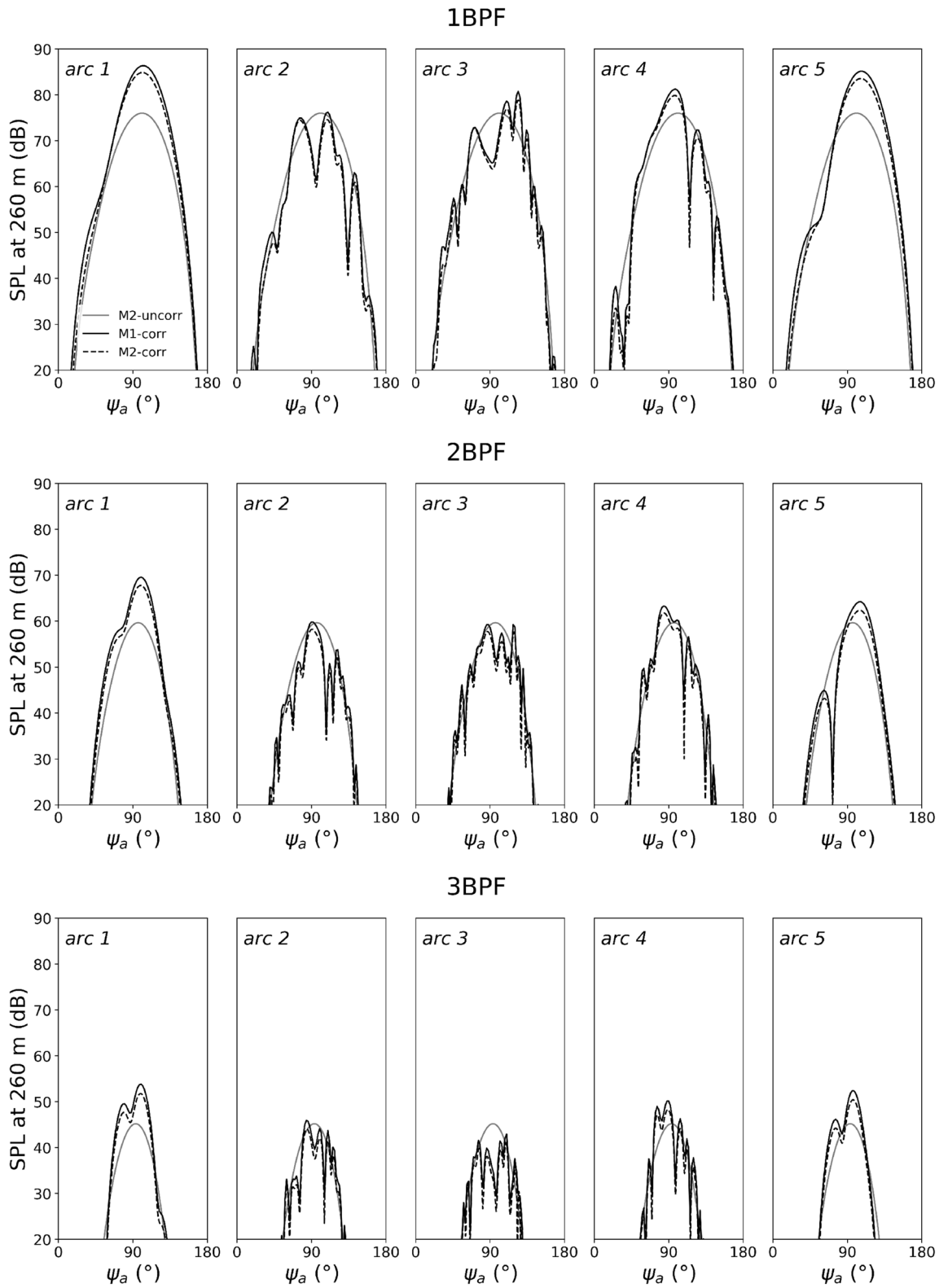

Fig. 19 SPL directivity along the five polar arcs defined in Fig. 18

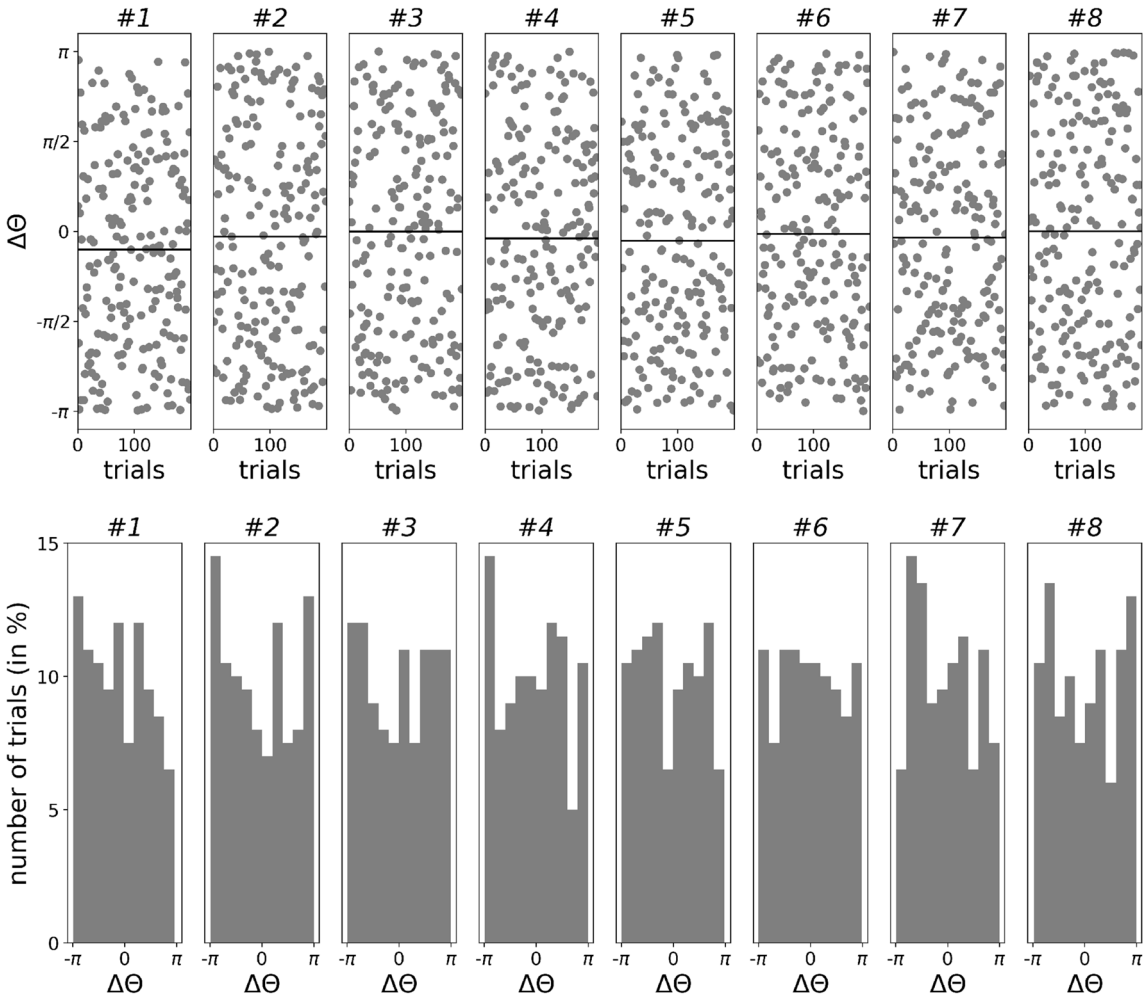

Fig. 20 For each of the 8 propellers, distribution of the values of initial position for the 200 trials

The results further indicate that the envelop of maximal value is below the theoretical increase of 9 dB with respect to the uncorrelated source case (compare gray solid lines and blue solid lines), which would be obtained if all the propeller contributions were added without any phase difference.

The distribution of $p_{\omega}^2|_{\Sigma corr}$ at 90° and for the BPF is shown in Fig. 22. The distribution is not symmetric. The positive skewness means that it is (slightly) more likely that the acoustic pressure amplitude is smaller than that obtained by assuming that all propellers are uncorrelated.

5 Conclusion

Two different and independent acoustic methods to predict propeller noise on the basis of RANS simulations were compared in this paper. Potentially, the first approach (fully numerical) is more accurate as it accounts for the fine details of the geometry and flow solution. It was demonstrated that the simplifications of the second method—dedicated to acoustic pre-design—do not significantly alter the results. This enabled the deeper investigation about the acoustic interference effect that was presented in the final part of the paper.

The directivity of the tones radiated by a single propeller is perfectly constant in azimuth and has the expected shape of an inverse parabola. In the meridian plane, the peak amplitude is located close to the zenith. The level at that position differs by less than 2 dB between both prediction methods. When the propellers are distributed along the (fictive) wing-span and their tonal emission is correlated, the directivity becomes three-dimensional and very complex because of the interference between the waves. Both prediction methods are in very good agreement also in that case.

In the last part of the paper, it was shown that the directivity patterns strongly change according to the values of initial

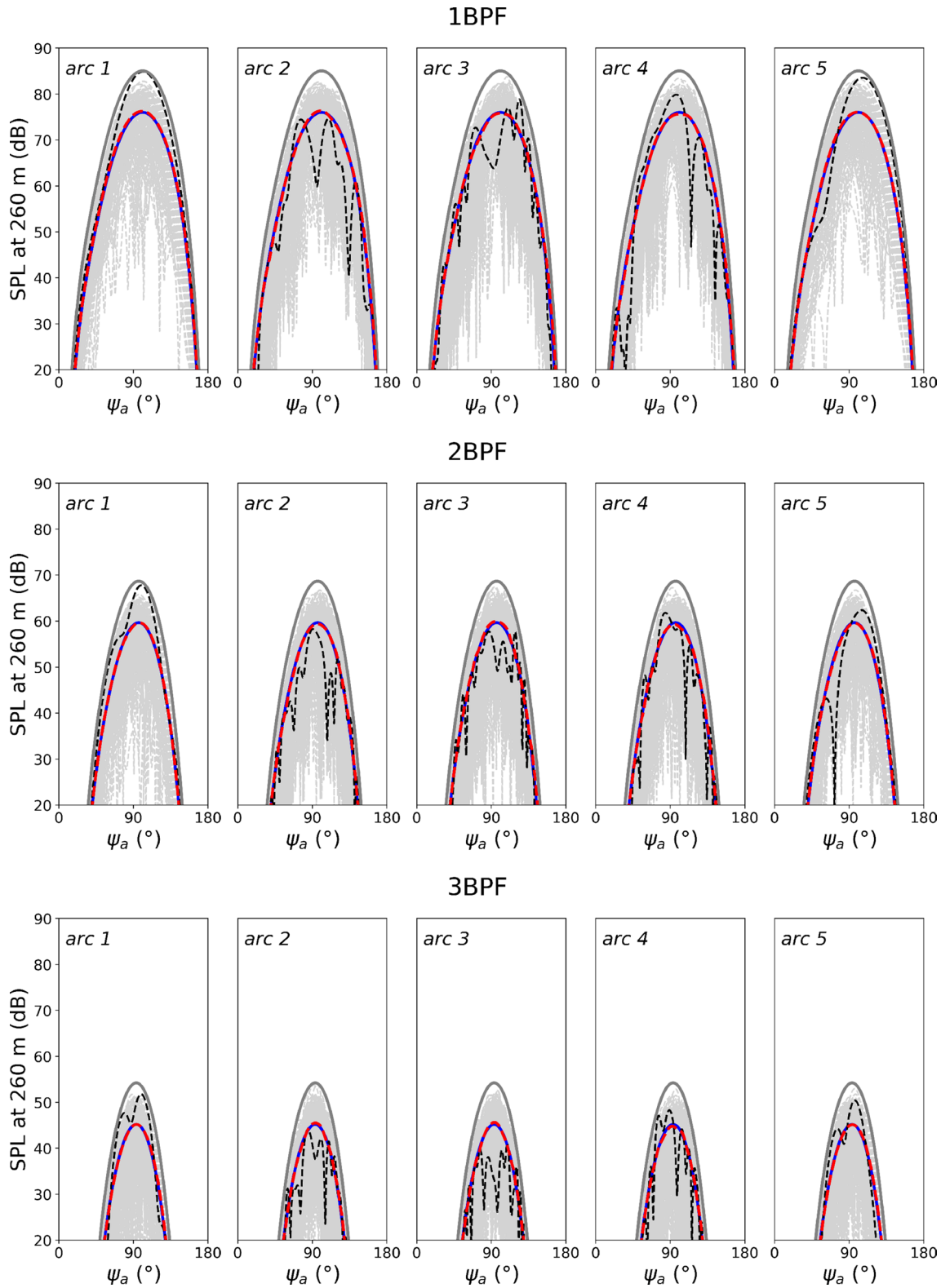

Fig. 21 Probability analysis: results on the sound directivity: (light gray solid lines) all 200 directivities, (red dashed lines) mean directivity, (blue solid lines) directivity assuming uncorrelated propellers, (gray solid lines) envelop of theoretical maximum, and (black dashed lines) directivity assuming identical propeller initial angular position

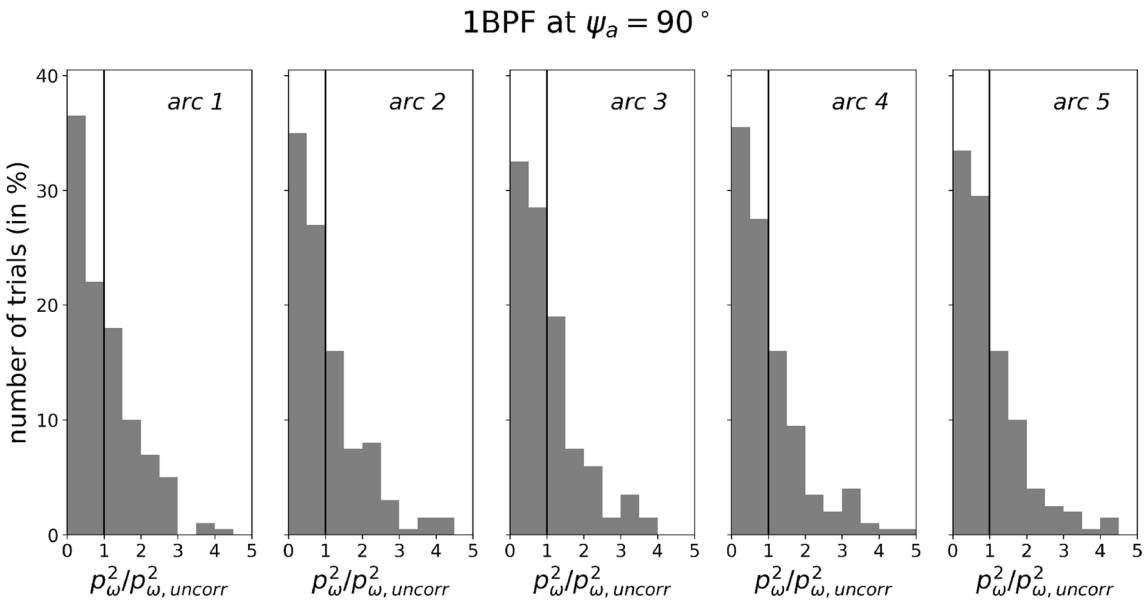

Fig. 22 Probability distribution of $p^2_\omega|_{\Sigma corr}$ for the 200 trials

relative angular position of the propeller blades. This constitutes a potential trap one should be aware of when working on distributed propulsion systems. It is highly recommended to anticipate this effect before conducting expensive numerical simulations. When the initial propeller positions are randomly varied according to the uniform probability density distribution model, the mean result (expectation) is the same as if the propellers were considered as uncorrelated. Finally, the results showed that the probability that the acoustic level is lower than the mean value is higher than 50% because of the positive skewness of the distribution of the resulting pressure amplitude.

Since the presence of the wing was not considered in this study, the legitimate question arises as to whether these findings remain true for a more realistic configuration. If a wing is included, the new unsteady sources of tones, which are created on the propellers and on the wings, are phase locked to the propeller. The same is true for the acoustic scattering by the wing. This means that a change in the initial angular position of the propellers directly translates into the same shift for the additional effects. Apart from the fact that the directivity pattern should change, the same dependency with respect to the relative propeller positions is expected. This remains to be demonstrated.

The consequences of neglecting the mutual aerodynamic interaction between the propellers can only be speculated upon. When the distance between the tips of the propellers is sufficiently small, it is expected that the noise emission per propeller, hitherto assumed to be unchanged regardless of the presence of the other propellers, will now vary as a function of the relative initial position of the propellers. If this were the case, the results of this study would no longer be entirely applicable. However, as this configuration would probably be noisier, it should be avoided in practice for regional aircraft.

Appendix

See Table 4.

Table 4 Propeller coordinates in the airplane reference frame

Propeller	Disk center coordinates		
	X (m)	Y (m)	Z (m)
1R	0.000	4.050	0.000
2R	1.318	7.358	−0.070
3R	1.637	10.666	−0.070
4R	1.955	13.974	0.290
1 L	0.000	−4.050	0.000
2 L	1.318	−7.358	−0.070
3 L	1.637	−10.666	−0.070
4 L	1.955	−13.974	0.290

Acknowledgements This work was conducted in the frame of the project IMOTHEP (Investigation and Maturation of Technologies for Hybrid Electric Propulsion), which has received funding from the European Union's Horizon 2020 research and innovation program under grant agreement No. 875006. The propeller considered in this work was designed by SAFRAN in the context of the H2020 project IMOTHEP. The authors are thankful to SAFRAN for providing the data needed for reproducing the blade geometry and validating the predicted propeller performances, thus providing a realistic test case for the application of the methodologies presented in the paper.

Funding Open Access funding enabled and organized by Projekt DEAL.

Data availability The data corresponding to the results of the study can be made available if requested.

Declarations

Conflict of interest The authors have no competing interests to declare that are relevant to the content of this article.

References

1. Intergovernmental Panel on Climate Change, Synthesis Report of the Sixth Assessment Report, https://www.ipcc.ch/ar6-syr/ Accessed 24 Feb 2023
2. Kim, H.D., Perry, A.T., Ansell, P.J.: pp. 9–11. , USA (2018). https://doi.org/10.2514/6.2018-4998
3. IMOTHEP (Investigation and Maturation of Technologies for Hybrid Electric Propulsion), https://www.imothep-project.eu/ (accessed 24 Feb 2023)
4. Guérin, S.., Moreau, A., A., Meier zu Ummeln, R., Staggat, M.: Parametric Study of the Noise Emitted by Uncorrelated, Distributed, Electric Fans, 2021 AIAA AVIATION Forum, Virtualement, 2021, https://doi.org/10.2514/6.2021-2137
5. Moore, K.R., Ning, A.: Takeoff and performance trade-offs of retrofit distributed electric propulsion for urban transport. J. Aircr. **56**(5), 1880–1892 (2019). https://doi.org/10.2514/1.C035321
6. Sgueglia, A., Schmollgruber, P., Bartoli, N., Atinault, O., Benard, E., Morlier, J.: pp. 8–12. , USA (2018). https://doi.org/10.2514/6.2018-1745
7. Sgueglia, A., Schmollgruber, P., Benard, E., Bartoli, N., Morlier, J.: Preliminary Sizing of a Medium Range Blended Wing-Body using a Multidisciplinary Design Analysis Approach, 8th EASN-CEAS International Workshop on Manufacturing for Growth & Innovation. MATEC Web of Conferences **233**, 00014 (2018). https://doi.org/10.1051/matecconf/201823300014
8. P. Schmollgruber, D. Donjat, M. Ridel, I. Cafarelli, O. Atinault, C. Francois, B. Paluch, Multidisciplinary Design and performance of the ONERA Hybrid Electric Distributed Propulsion concept (DRAGON), AIAA Scitech: Forum, 6–10 January 2020, Orlando, (FL). USA (2020). https://doi.org/10.2514/6.2020-0501
9. de Rosa, D., Morales Tirado, E., Mingione, G.: Parametric investigation of a distributed propulsion system on a regional aircraft. Aerospace (2022). https://doi.org/10.3390/aerospace9040176
10. Minervino, M., Andreutti, G., Russo, L., Tognaccini, R.: Drag reduction by wingtip-mounted propellers in distributed propulsion configurations. Fluids (2022). https://doi.org/10.3390/fluids7070212
11. Bernardini, G., Centracchio, F., Gennaretti, M., Iemma, U., Pasquali, C., Poggi, C., Rossetti, M., Serafini, J.: Numerical characterisation of the aeroacoustic signature of propeller arrays for distributed electric propulsion. Appl. Sci. (2020). https://doi.org/10.3390/app10082643
12. de Vries, R., van Arnhem, N., Sinnige, T., Vos, R., Veldhuis, L.L.M.: Aerodynamic interaction between propellers of a distributed-propulsion system in forward flight. Aerosp. Sci. Technol. (2021). https://doi.org/10.1016/j.ast.2021.107009
13. Pascioni, K., Rizzi, S.A.: Tonal Noise Prediction of a Distributed Propulsion Unmanned Aerial Vehicle, 2018 AIAA/CEAS Aeroacoustics Conference, Atlanta (GA), USA, June 25-29 2018, https://doi.org/10.2514/6.2018-2951
14. Poggi, C., Rossetti, M., Serafini, J., Bernardini, G., Gennaretti, M., Iemma, U.: Neural network meta-modelling for an efficient prediction of propeller array acoustic signature. Aerosp. Sci. Technol. (2022). https://doi.org/10.1016/j.ast.2022.107910
15. Block, P.J.W.: Experimental study of the effect of installation on single- and counter-rotation propeller noise, NASA Technical Paper 2541 (1986)
16. Tormen, D., Giannattasio, P., Zanon, A., De Gennaro, M., Kühnelt, H.: Semi-analytical tip vortex model for fast prediction of contrarotating open rotor noise. AIAA J. **59**(5), 1629–1644 (2021). https://doi.org/10.2514/1.J059314
17. Brentner, K., Farassat, F.: Analytical comparison of the acoustic analogy and Kirchhoff formulation for moving surfaces. AIAA J. (1998). https://doi.org/10.2514/2.558
18. Moreau, A., Guérin, S.: Similarities of the in-duct and free-field formulations in rotor noise problems, 17th AIAA/CEAS Aeroacoustics Conference (32nd AIAA Aeroacoustics Conference), pp. 05–08. Portland, USA (2011). https://doi.org/10.2514/6.2011-2759
19. Moreau, A.: A unified analytical approach for the acoustic conceptual design of fans of modern aero-engines, Technische Universität Berlin, 2017, Dissertation
20. Hanson, D.B.: Helicoidal surface theory for harmonic noise of propellers in the far field. AIAA J. (1980). https://doi.org/10.2514/3.50873
21. Guérin, S., Moreau, A., Menzel, C., Weckmüller, C.: pp. 04–06. , USA (2012). https://doi.org/10.2514/6.2012-2303
22. Willmarth, W.W., Roos, F.W.: Resolution and structure of the wall pressure field beneath a turbulent boundary layer. J. Fluid Mech. (1965). https://doi.org/10.1017/S0022112065000599